

Preclinical-grade microendoscope for optical coherence tomography and angiography inside the bladder

Gerardo González-Cerdas¹,^{a,*} Yanis Taege¹,^a Felix Jund¹,^a
Dragan Sandic,^b Christoph Bauer,^b and Çağlar Ataman¹^c

^aUniversity of Freiburg, Gisela and Erwin Sick Chair of Micro-Optics,
Department of Microsystems Engineering, Freiburg, Germany

^bBlazejewski MediTech GmbH, Sexau, Germany

^cUniversity of Freiburg, Microsystems for Biomedical Imaging Laboratory,
Department of Microsystems Engineering, Freiburg, Germany

Abstract. We present a preclinical-grade, forward-viewing endomicroscope for in-contact optical coherence tomography (OCT) and optical coherence angiography (OCA) imaging through the working channel of a conventional cystoscope. Beam scanning is achieved with a fiber scanner driven by a tubular piezoelectric actuator. A focusing lens at the fiber tip helps engineering of the operation frequency within a compact probe length to avoid lateral undersampling. Microstructuring of fused silica through selective laser-induced etching was used for manufacturing a self-aligning housing for the probe head. The entire micro-optical system is assembled and encapsulated within a custom-developed sterilizable packaging with 4.5 mm outer diameter. The presented design and fabrication strategy can be used for any forward-viewing probe, independent of its imaging modalities. We demonstrate OCT imaging within a 2.1-mm diameter field of view at a transverse resolution of 19 μm and microvasculature visualization through OCA. The presented probe's mechanical characteristics and optical performance make it particularly attractive for outpatient care use in the detection of tissue pathology inside the bladder. The presented fabrication methodology provides a reliable strategy for enabling preclinical trials with endoscopic imaging probes. © The Authors. Published by SPIE under a Creative Commons Attribution 4.0 International License. Distribution or reproduction of this work in whole or in part requires full attribution of the original publication, including its DOI. [DOI: [10.1117/1.JOM.3.1.011006](https://doi.org/10.1117/1.JOM.3.1.011006)]

Keywords: endomicroscopy; biophotonics; optical coherence tomography; optical coherence angiography; bladder cancer; micro-optics.

Paper 22024SS received Oct. 11, 2022; accepted for publication Jan. 16, 2023; published online Jan. 31, 2023.

1 Introduction

Each year, more than 18 million new cases of cancer are diagnosed worldwide, with urinary bladder cancer (UBC) accounting for approximately half a million of them, positioning it among the top ten most common cancer types.¹ Additionally, UBC has the highest lifetime treatment costs per patient of all cancers,^{2,3} partially due to high recurrence rates and the associated intensive surveillance strategies.⁴ Since recurrence rates seem to vary significantly depending on the grade and number of tumors,^{5,6} improvements to the diagnosis and surveillance procedures can significantly reduce both health care costs and patient discomfort. Currently, diagnosis and screening of UBC involves inspection of the bladder tissue through white light cystoscopy, commonly followed by excisional biopsy and histological analysis. Adoption of different imaging modalities, however, is an active field of study, since advanced photonic imaging methods can be used to visualize and assess the state of the tissue *in vivo*, looking for specific biomarkers that can provide information previously inaccessible *in situ*. Furthermore, such modalities could be implemented in a device that can be inserted through the same working channel commonly used for excision tools.

*Address all correspondence to Gerardo González-Cerdas, gerardo.goncer@gmail.com

Optical coherence tomography (OCT), a volumetric imaging technique that provides detailed subsurface morphological tissue information, has been shown to be a useful tool for detection and grading of nonmuscle-invasive bladder cancer, particularly when combined with complementary imaging modalities.^{7,8} One such modality, which is in fact a functional extension of OCT and therefore uses the same hardware, is optical coherence angiography (OCA), which images tissue microvasculature in 3D. Given the irrigation needs of cancerous tumors, such vascularization data can aid the clinician in detecting their presence, especially when correlated with morphological images of static tissue from OCT. Previous works have presented OCT and OCA implementations in endoscopic instruments for other tissue types, highlighting their potential for clinical settings,^{9,10} but further trials are still required before these endomicroscopes can become a regular part of the outpatient care standard. There is a clear need, then, for instruments that are not only able to provide high-resolution OCT and OCA images, but also meet the stringent regulations and approval processes for medical-grade devices.

In this work, we discuss the design, implementation, and preliminary experimental evaluation of a forward-looking OCT and OCA probe with preclinical-grade encapsulation, designed to be used through the working channel of a rigid cystoscope for early detection of UBC. Volumetric imaging is achieved by a miniaturized piezoelectric-based fiber scanner, which is only 11.5 mm long, making future implementations in flexible endoscopes possible. The lens holder, scanner housing, and self-alignment structures for the probe head assembly are manufactured via selective laser-induced etching (SLE), a 3D glass microstructuring technology that enables the creation of alignment, pinning and interconnecting features with micrometer precision.¹¹ Through experimental results, we demonstrate that the endomicroscope can provide OCT tomograms and OCA vascularization projections with a circular field of view (FOV) of up to 2.1 mm and a transverse resolution of 19 μm . The same performance parameters are measured both before and after a series of standard sterilization procedures, proving the potential of the system as a reusable endomicroscope.

2 Optomechanical Design and Medical-Grade Encapsulation

The design space for any endomicroscopy probe is predominantly defined by the maximum physical dimensions allowed by the working channel of the mother endoscope. The probe developed in this work is for rigid cystoscopy, and thus there is no defined upper limit on the length of the rigid end (e.g., probe head). The maximum outer diameter was defined as 4.5 mm to ensure a comfortable fit into the working channel of the cystoscope, which had a circular cross-section working channel of 5 mm. To comply with the safety protocols of a clinical setting and provide enough maneuverability to the operator, the distal length of the instrument was defined as 3.8 m. All the optical functionality is packed in a 3D microstructured probe head machined from fused silica, which constitutes most of the rigid distal end of the microendoscope. This core unit is protected by encapsulation that allows multiple sterilization runs, making the total rigid tip 18.5 mm long. The proximal sections provide the optical and electrical interfacing with the system's back end. Figure 1 shows a (shortened) CAD model of the entire probe, described in more detail throughout this section.

For *in vivo* use, the probe must also comply with regulations that ensure the safety of both the subject and the operators of the system. We have, therefore, developed a complete encapsulation approach that meets the biocompatibility, hermeticity, and electromagnetic interference criteria defined in medical standards IEC 60601-1-2, by adapting industry-standard materials and procedures to our endomicroscope. This encapsulation solution has already been successfully tested under a standard hydrogen-peroxide gas plasma sterilization process (STERRAD[®]), with the device performing comparatively as well after five sterilization cycles, as shown later in Sec. 4.2.

2.1 Probe Head and Distal Section

A detailed description of the design requirements and implementation of the probe head itself has been given by the authors in Ref. 12 and is summarized here for completeness. Since OCT is a scanned imaging technique, the probe head needs to feature a miniaturized laser scanner.

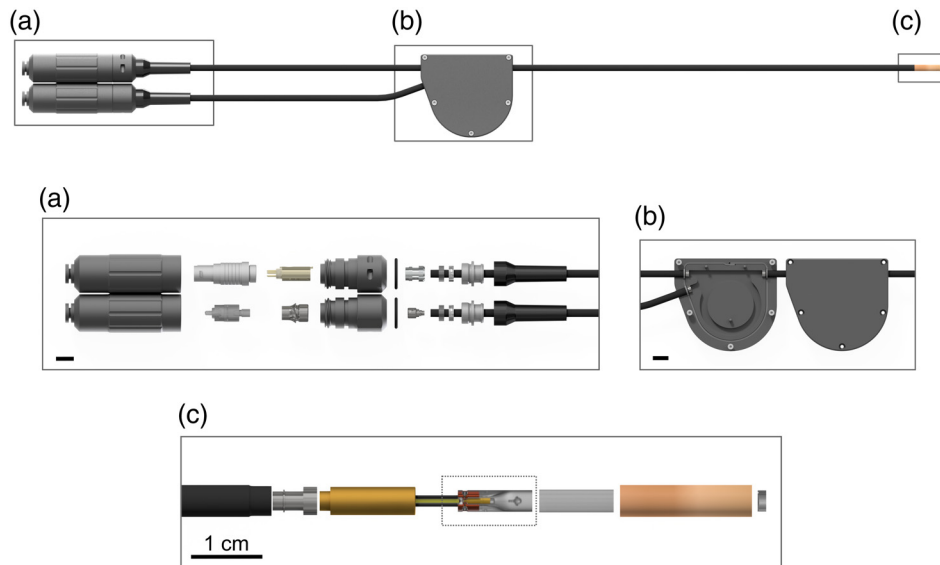


Fig. 1 Computer-aided design of the microendoscope, highlighting its three main sections: (a) the proximal side connectors that interface with the back end of the system, (b) a cable-splitter junction that separates the distal and proximal sides, and (c) the distal end which contains the functional core unit or probe head (dotted box). The probe length is not shown to scale. All scale bars are 1 cm.

For nontubular hollow organs, such as the urinary bladder, forward viewing illumination is the most appropriate. Thus 2D scanning is implemented with a fiber-based cantilever scanner, actuated by a piezoelectric tube and driven in a quasiresonant state.^{13,14} Furthermore, the probe needs to be operated in contact with the tissue to avoid motion artifacts in OCA imaging. The fiber deflection and sizes of the focusing optics were selected to maximize the FOV while staying within the design limitations dictated by the diameter of commercial cystoscopes' working channels.

Figure 2 shows a schematic view of the probe head optomechanics, and a summary of the target specifications is shown in Table 1. The scanner works as follows: By applying a sinusoidal voltage to the outer electrodes of the piezotube (PIC151 from PI) with a frequency close to the cantilever's first natural frequency, a fast circular motion of the beam is achieved, generating a ring-shaped scan at the focal plane. An additional modulation signal with a much lower frequency (in the range of 0.5 to 2 Hz) is used to envelop the excitation signal, such that the size of the illumination ring oscillates, effectively creating a spiral pattern that grows and shrinks, where each "ring" of the spiral corresponds to a 2D image (OCT B-scan), and one complete spiral generates a 3D cylindrical volume (OCT C-scan).

Since the scan time for every ring in the spiral pattern is constant, due to the quasiresonant operation, spatial sampling is nonuniform. Furthermore, the spatial sampling rate is also limited by the repetition rate of the swept-source featured in the OCT system. To maintain a Nyquist sampling rate and ensure an optics-limited resolution even for the largest rings of the spiral scan pattern, the operation frequency should be sufficiently small. By accommodating the focusing

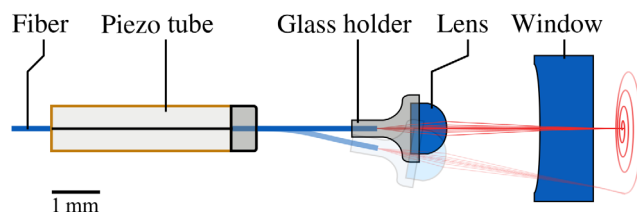


Fig. 2 Schematic of the piezo-based fiber scanner. The front window allows for operation in contact with the tissue, essential for OCA. Image adapted from Ref. 12.

Table 1 Optomechanical design parameters of the OCT/A endomicroscope.

Parameter		Design value
Operation wavelength	λ	1.3 μm
Laser sweep frequency		173,611 Hz
Numerical aperture	NA	0.04
Transverse resolution	Δx	19 μm
Axial resolution (air)	Δz	5.1 μm
Working distance	WD	500 μm
Depth-of-field (FWHM)	DOF	1.06 mm
Resonance frequency	f_{res}	300 Hz
C-scan rate OCT/OCA		$1/N + 1$ s
Max. optical aperture		2.7 mm
Glass housing diameter		3.0 mm
Distal rigid length		18.5 mm
Maximum outer diameter		4.5 mm

lens at the fiber tip via a glass holder, both the optical resolution and the operation frequency can be engineered according to the specifications of the OCT back end. The negative lens at the distal end both seals the probe-head and increases the total FOV. In this particular design, the window is mounted on the outer cap, to maintain the overall diameter of the probe within design requirements.

To map the acquired images on a uniform sampling grid, an open-loop spiral calibration step is necessary before every set of measurements.¹⁵ This is needed to record the real trajectory of the beam, since every scanner has a slightly different mechanical response, which can also drift due to temperature changes. To address this, a calibration engine that can be included in the instrumentation rack has been developed, to facilitate a quick calibration (<2 min) before every patient is examined. Previous works^{7,16} with similar piezoelectric-based probes have demonstrated this approach to be sufficient for extended measurement sessions (> 20 min). Nevertheless, a direct-feedback mechanism to continuously register the actual trajectory traced by the beam spot would be a more desirable solution.

The optomechanical components comprising the functional unit from Fig. 2 are mounted on a glass platform, which is explained in more detail in Sec. 3.2. This glass housing provides a precise and practical solution for assembly, but it cannot guarantee the level of robustness necessary for a clinical study, since cystoscopy procedures require that the endomicroscope goes through standard disinfection and sterilization processes, as well as increased mechanical stress from manipulation inside the body. We have, therefore, adapted the design of the glass housing and the assembly procedure of the entire probe to include an additional layer of encapsulation that meets such requirements.

Figure 3 depicts an exploded view of the distal end of the endomicroscope, including all encapsulation components. The encapsulation starts with a distal cover (2) made out of poly-ether ether ketone (a thermoplastic polymer), in which the front window (1) is fixed, ensuring a hermetic seal at the contact point with the tissue. The glass probe head (4) is partially covered by an isolating foil (3) to protect against electrical breakdown of the piezotube electrodes and a brass tube (5) provides electro-magnetic shielding. A metal flange (6) is used for a secure mechanical coupling with a stainless-steel helix located inside of the outer silicone tube (7), through which the wires and optical fiber are guided to the proximal end of the device.

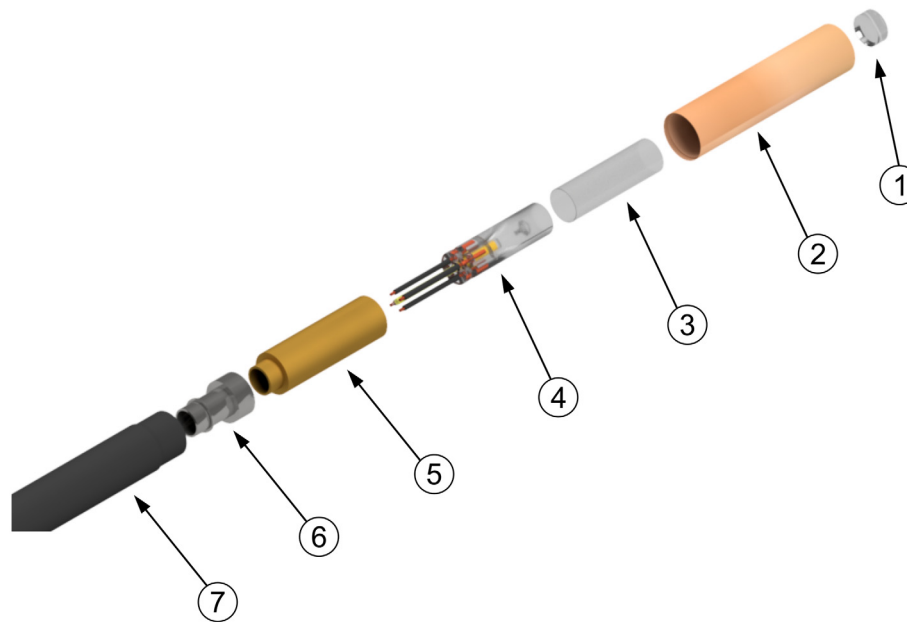


Fig. 3 Exploded view of the distal-side encapsulation for the endomicroscope, showing (1) the sealing window, (2) outer cap, (3) isolation foil, (4) functional probe head, (5) shielding tube, (6) mechanical coupling, and (7) outer tubing.

2.2 Proximal Section

On the proximal side, as shown in Fig. 4, a sealed splitter junction (a) is used to separate the cables and the fiber for interfacing with the instrumentation rack. The fiber is coiled inside the splitter to preserve its minimum bending radius, and a silicone gasket (1) ensures a hermetic seal. Two shorter sections of tubing lead to the proximal connections (b). Here strain relief boots (2) cover the mechanical coupling parts (3) for the instrumentation connectors. End stoppers with integrated seal rings (5 and 4, respectively) protect the interface between fiber/cables and connectors from pulling forces and overbending. The FC/APC (6) and LEMO (7) connectors, for the optical and electrical signals, respectively, can be covered with sealing caps (8) to protect them during the disinfection and sterilization processes.

3 Fabrication and Assembly

3.1 Manufacturing of the Probe Head Assembly Platform

The optomechanical components comprising the probe head are assembled on a glass platform, which also acts as the first level of encapsulation. This was fabricated through SLE (LightFab GmbH), a two-step subtractive 3D microstructuring process that can provide a selectivity of up to 1:1500.¹⁷ With a precision that can attain 1 to 5 μm depending on the specific structure, it allows for optomechanical designs that can be precisely tuned during production and assembly, facilitating the mounting and interconnection of components to provide a robust fabrication process.^{11,12,18} To reach such tight fabrication tolerances, both the laser-writing and chemical etching steps of the process need to be fine-tuned through various iterations, which can be time-consuming and is not suitable for fast prototyping. However, once the appropriate control parameters have been found for a specific design, it can be easily replicated in batch. For the probe head platform presented here, the laser-marking time was approximately 2.5 h per unit. Etching time for a batch of 24 units was around 16 h at 80°C, although more units can be etched simultaneously. The maximum size of any individual glass part is limited by the lateral dimensions of the mechanical stage and the maximum substrate thickness suitable for the focusing objective (10 × 14 cm and 5 mm in our case, respectively). Making use of this glass housing

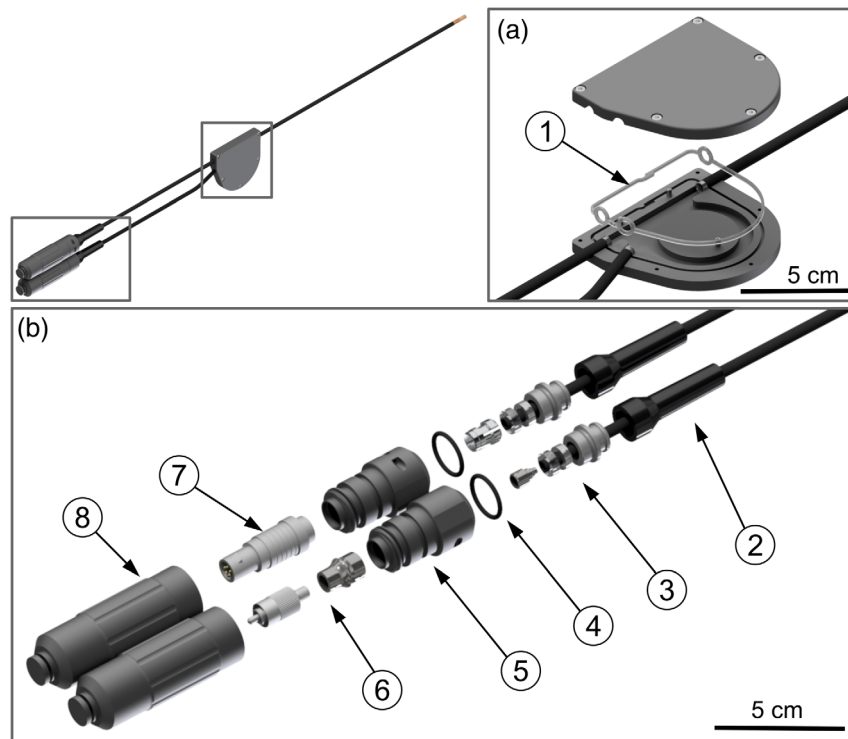


Fig. 4 Exploded view of the proximal-side encapsulation for the endomicroscope. Inset (a) shows the cable splitter junction with its sealing gasket (1), whereas (b) depicts the strain relief (2), mechanical couplers (3), and end-stoppers (4), (5) for the optical (6) and electrical (7) connectors, along with their protective caps (8). The probe length has not been rendered to scale.

results in a functional probe head that is slightly larger in diameter than its largest optical component.

3.2 Probe Assembly

Figure 5 depicts a 3D render of the probe head assembled on the glass platform. The first assembly step is the placement and fixing of the piezoelectric tube onto the housing. Since there are no optical components at the proximal side of the scanner (other than the fiber itself),

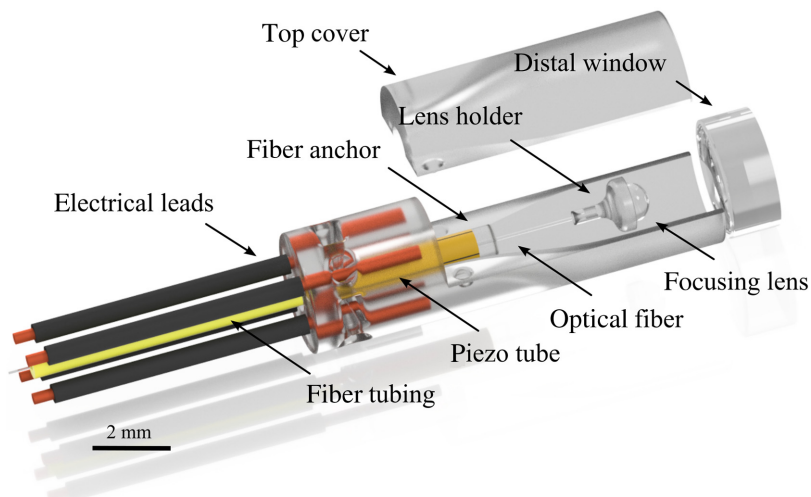


Fig. 5 CAD render of the bare OCT/A probe head.

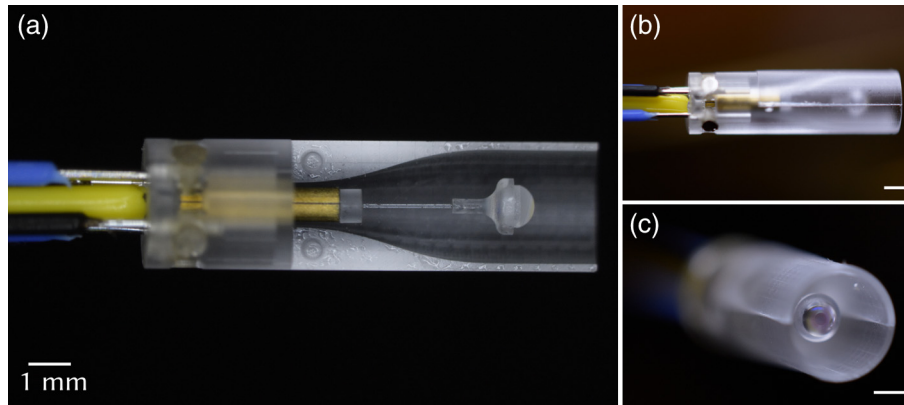


Fig. 6 Photographs of a completed scanner without encapsulation, showing (a) top, (b) side, and (c) angled views of the probe head. Scale bars = 1 mm.

there is enough available space in the housing for creating holding, alignment, and interconnection features. An auxiliary structure was also manufactured to aid in the assembly of the glass holder and the focusing lens on the fiber tip, as previously presented by the authors in Ref. 12 and 18. The streamlined and precise process enabled by this approach allows for an increase in fabrication yield and reduces the assembly time, as well as the risk of damage or misalignment during the critical fixing steps. Figure 6 shows a complete probe-head before finalizing the probe's encapsulation. It should be noted that the probe-head assembly is performed once all electrical and optical lines are guided through the outer encapsulation, to minimize mechanical strains on the assembly. The distal window is mounted and sealed in the outer cover of the probe head.

Figure 7 shows the complete endoscopic probe. The distal length of the endomicroscope is 3.8 m (with a total length of 4 m), providing good maneuverability for the operator during the endoscopic procedure, and allowing for the instrumentation rack to be located at a safe distance inside of the operating theater.



Fig. 7 Photographs of completely encapsulated OCT/A probes, showing the proximal (a) end connectors, (b) the scale of the 4.5-mm distal end, and (c) the probe introduced into a commercial cystoscope.

4 Experimental Evaluation

4.1 OCT System

The OCT system used for imaging with the presented probe features an akinetic tunable source (Insight Photonic Solutions, USA: Atlas akinetic laser) with a central wavelength of 1310 nm, a bandwidth of up to 90 nm and a maximum output power of 60 mW. To keep signal-to-noise ratio (SNR) levels from the laser high, A-scan rate is limited to 173 kHz, but it can be increased to up to 180 kHz.

4.2 Optomechanical Characterization

For both OCT and OCA, a suitable operating point for the probe needs to be found where a large FOV can be achieved while maintaining a stable scanning pattern. Table 2 summarizes the measured optical performance parameters for the probe at the chosen operating frequency, both before and after going through five cycles of hydrogen peroxide sterilization. Although some deviations could be measured in the probe's behavior after sterilization, they lie within tolerance and do not necessarily represent degradation, as a similar variance can be seen in nonsterilized probes as well. OCT images of skin tissue taken before and after sterilization were also of comparable quality.

Figure 8 shows the deflection of the fiber tip along one of the cantilever's axes for a frequency sweep of the excitation signal applied to the electrodes (for a given voltage amplitude). Before sterilization, the resonance peak was found to be at around 303 Hz, so a driving frequency of 306 Hz was chosen for a quasiresonant operation with reduced phase sensitivity. To evaluate the repeatability and stability of the scan pattern, which is of particular importance for OCA, 18 patterns were acquired in succession. A standard deviation below $7 \mu\text{m}$ was measured for

Table 2 Inspected parameters before and after sterilization.

Parameter		Before sterilization	After sterilization
Scanner resonance frequency (Hz)	f_{res}	303	307
FOV (mm)	FOV	2.1	1.9
Back reflections (ppm)	BR	34.88	46.67
SNR	SNR	94 dB	Did not change
Scan-to-scan deviation	σ_x	$<7 \mu\text{m}$	Did not change
Visual inspection		No visible damage	No visible damage

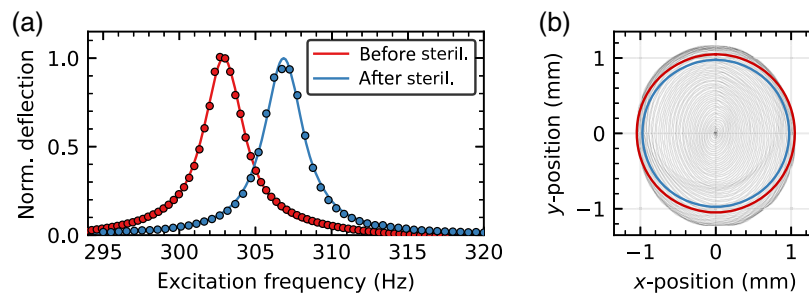


Fig. 8 Results of the mechanical characterization of the probe: (a) normalized maximum lateral deflection of the cantilever's tip as a function of the driving frequency for a single axis and (b) scan pattern obtained by the PSF. Due to the slightly asymmetric profile, the effective FOVs are marked by colored circles.

three arbitrary points along the spiral pattern across the 18 samples. At the chosen operating point, a stable and reproducible scan pattern with an FOV of up to 2.1 mm could be achieved, which was recorded for 3D reconstruction and is also shown in Fig. 8.

4.3 OCT Imaging

The quality of the OCT images depends heavily on the sample properties and measurement environment. In turn, detecting microvascular structures from the OCT data requires maximizing both contrast and signal quality. Parasitic back reflections from inside the probe, stemming from different optical interfaces in the imaging path, impact the OCT signal quality by reducing the SNR, so they must be minimized during assembly. Some of them, however, such as the interface between glass and air for the focusing lens and front window, are always present, so the reference arm of the OCT setup needs to be adjusted to position the signal from the sample outside of parasitic lines. Since the penetration depth inside tissue is limited by scattering to around 1.5 mm, the complete signal can be imaged unobstructed, although the effect of parasitic back reflections is still observable, as they raise the noise floor.

Since the probe has been designed for operation inside the bladder, it is optimized for imaging in water (cystoscopies are normally performed in a hydrodistended bladder). Clinical trials were out of the scope of this work, and excisional bladder tissue cannot be used for OCA because blood flow is required, so *ex vivo* measurements were taken on human skin and buccal mucosa of a healthy volunteer. Informed written consent was obtained prior to the experiment, and the study was in agreement with the tenets of the declaration of Helsinki and approved by the Institutional Ethics Committee. As shown in Fig. 9, dry skin gives a strong reflection from the window and tissue surface, resulting from the air interfaces, whereas wet skin results in a better contrast due to a reduced initial reflection at the surface. The image from the inner lip also shows a low surface signal, with strong contrast deep into the tissue. For angiographic image acquisition, the inner lip was chosen, as it showed the best OCT images and has more blood vessels close to the surface. The OCT images shown correspond to raw B-Scans, and it is worth mentioning that increasing

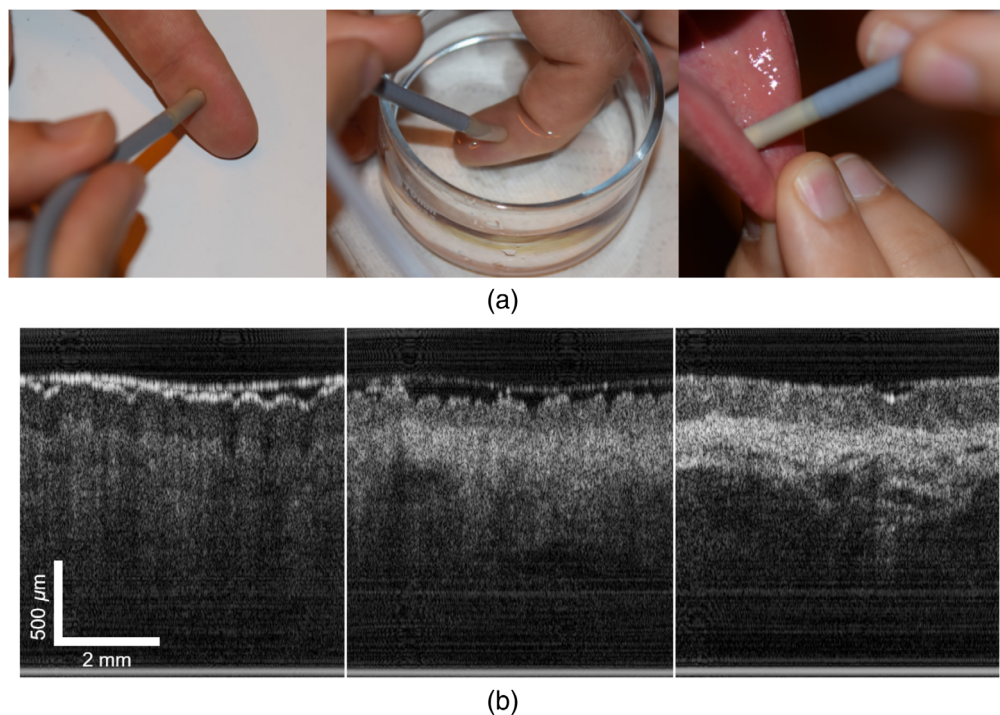


Fig. 9 (a) Measurement conditions of different samples on dry skin, wet skin, and wet soft tissue, from left to right. The probe is sealed and sterilized, allowing measurements under water and inside the mouth. (b) Corresponding OCT B-scans of dry skin, wet skin, and wet soft tissue, from left to right.

the SNR of the back-end system or applying contrast-enhancing postprocessing to the images can improve their quality.

4.4 OCA Imaging

OCA is a functional extension of OCT that monitors speckle contrast between consecutive tomograms acquired on the same location.^{19,20} In live tissue, if the consecutive tomograms are acquired within sufficiently short intervals, the main source of contrast is blood flow, rendering microvasculature imaging possible without additional hardware.

4.4.1 OCA with a spiral scanner

To minimize the time between consecutive tomograms, the correlation analysis is performed over multiple elliptical B-scans with radial spacing significantly smaller than the optical resolution.^{10,21} For this purpose, the modulation frequency for the spiral scanner is decreased to a fraction of that used for OCT, effectively reducing the volume rate by the same factor. As explained in the next section, the C-scan time for OCA is therefore increased to $N + 1$ seconds, where $N = 4$ showed to be a reasonable compromise between acquisition time and image quality.

4.4.2 OCA data analysis

In addition to the scanning scheme, there are multiple approaches to obtaining angiography images from OCT data. The operating principle of OCA relies on the fact that static tissue will always provide the same interference speckle pattern in the OCT signal over time, whereas dynamic features (such as blood vessels with a flow of large cells inside) will generate a signal that can change between measurements. In this work, we used two different algorithms to monitor intensity variations between tomograms. The first one is a simple implementation called speckle variance (SV), which repeats the B-scans N times at the same location and calculates the standard deviation of the intensity I_{SV} as²²

$$I_{SV} = \frac{1}{N} \sum_{i=1}^N \left(I_{ijk} - \frac{1}{N} \sum_{i=1}^N I_{ijk} \right)^2, \quad (1)$$

where I_{ijk} is the measured intensity at depth j and position k of the i 'th B-scan.

The second method calculates a correlation parameter between A-scans, with static tissue having a high correlation and flow leading to a lower correlation.²³ To enhance the contrast by suppressing speckle-dependent noise, split-spectrum amplitude-decorrelation angiography (SSADA) divides the full OCT spectrum into smaller bands. A decorrelation parameter $D(x, z)$ is calculated based on the intensity $I(x, z)$ of the N B-scans split into M spectra each,²⁴ so that

$$D(x, z) = 1 - \frac{1}{N-1} \frac{1}{M} \sum_{n=1}^{N-1} \sum_{m=1}^M \frac{I_{n,m}(x, z) I_{n+1,m}(x, z)}{\left[\frac{1}{2} I_{n,m}(x, z)^2 + \frac{1}{2} I_{n+1,m}(x, z)^2 \right]}. \quad (2)$$

To calculate SV, N A-scans are used, whereas SSADA uses $N \cdot M$ A-scans. For angiographic images, depth projections are of particular interest, showing the vascular structures from a top view. An axial region of interest can then be displayed as either an average intensity projection or a maximum intensity projection, as shown in Sec. 4.5.

4.5 OCA Results

Both SV and SSADA were tested with various input parameters. For better visualization and comparison, the data have been reconstructed and processed into a depth projection. Figure 10 exemplifies this, showing both an OCT and OCA B-scan obtained through SV, with

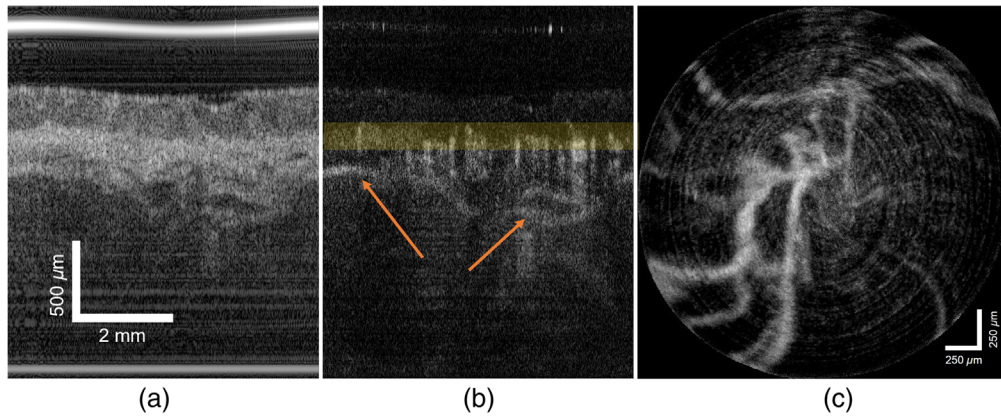


Fig. 10 Data acquired with SV and $N = 4$: (a) OCT image, (b) OCA image, and (c) 2D reconstructed top-view at the depth indicated in yellow in the OCA image. Arrows point at possible noise signals at the deeper layers. Microvascular structures can be identified with continuous vessels. Individual rings with higher noise level can be seen in the reconstruction.

a related average intensity depth projection over $\approx 86 \mu\text{m}$. The concentric rings visible in the reconstruction are the result of intensity variations in the OCT signal coming from static tissue across multiple B-scans, most likely due to motion artifacts or slight power oscillations from the source. Additionally, a vessel can be seen in light gray that ends unconnected to the rest, probably due to a low sensitivity for thinner vessels. A higher N might improve the sensitivity, but it would also increase the impact of bulk motion.

Figure 11 shows OCA images obtained through SV where N equals 2, 4, and 6. The lower sensitivity of a low N can be seen in the fading ends of some vessels. However for $N = 6$, the vessels of lower signal are cut through by several rings with overall low signal. A trade-off between sensitivity and noise due to movement as a result of a longer acquisition time must be taken into account when choosing N . For $N = 4$, a total scan time of 5 s results in a reasonable

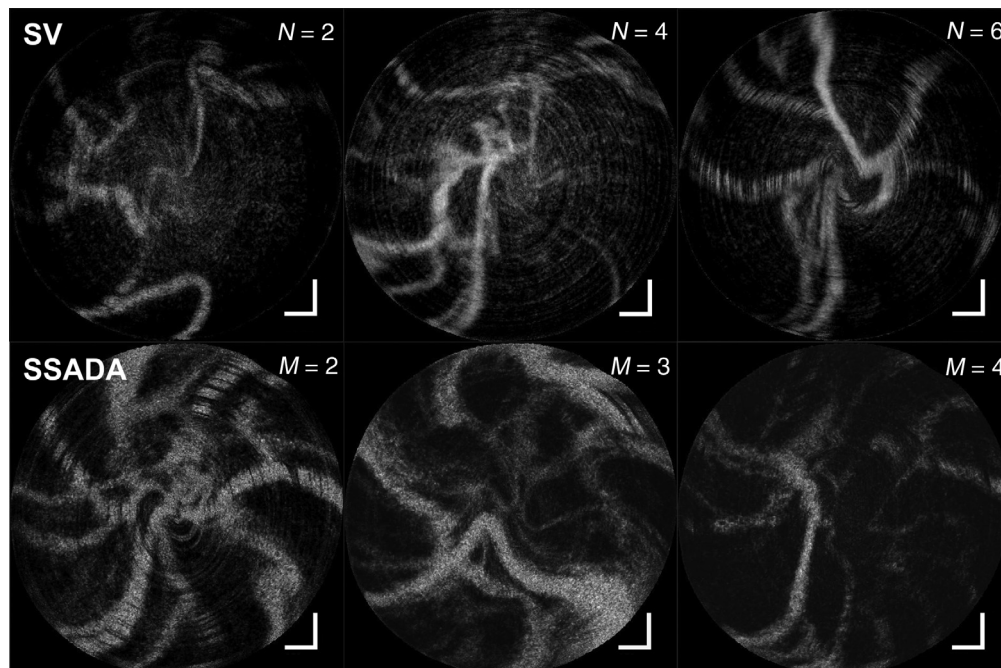


Fig. 11 Depth projections of OCA images obtained through SV, with different values of N , and through SSADA, with $N = 4$ and different values for M . All scale bars are $250 \mu\text{m}$.

quality. This number is then used as the basis for measurements processed with SSADA, also shown in Fig. 11.

SSADA can improve the SNR of OCA images, as all B-scans are averaged M times before calculating the decorrelation signal. As the data are shown as a top-view depth projection, the reduced axial resolution plays a less significant role. Due to the increased computing power needed with increasing M , it is limited to four split bands. Although individual rings can still be seen for $M = 2$, they are less significant and then disappear completely for higher values. Background noise is also significantly reduced, as the averaging of B-scans lowers the noise and therefore increases the correlation for static tissue.

In general, the noise observable in the final OCA images is most likely due to scan repeatability issues, which is hard to address in piezo-based scanners and causes problems with speckle decorrelation algorithms. Improvements in the stability of the scanner by modifying the enveloping function or through a direct feedback mechanism for better control of the scan pattern could improve the image quality. Additionally, turning to other methods that do not rely only on speckle decorrelation could alleviate this problem.

5 Conclusions

The compact, preclinical-grade probe presented in this work represents a key step toward expanding the use of endoscopic OCT systems for outpatient care, specifically in the detection and surveillance of bladder cancer. The depth maps that can be constructed from the OCA data acquired with the presented process can prove to be a valuable addition to the noninvasive endoscopic OCT, providing complementary data and expanding the probe's capabilities for optical biopsy.

The optical performance and medical-grade encapsulation of the instrument illustrate design and implementation methodologies capable of producing a reliable and safe operation in the clinic. These principles provide a strong reference and proof of concept for the continuous development of multimodal endoscopic imaging tools, which can be adapted to other pathologies and tissue types.

Acknowledgments

This work has received funding from the European Union project MIB (Horizon 2020, Grant Agreement No. 667933). The authors would like to thank F. Placzek, R. Leitgeb, and W. Drexler from the Center for Medical Physics and Biomedical Engineering of the Medical University of Vienna, for their guidance and assistance in implementing the OCT system used in this work. The authors declare to have no relevant financial interests in the manuscript and no other potential conflicts of interest to disclose.

References

1. A. Richters, K. Aben, and L. Kiemeny, "The global burden of urinary bladder cancer: an update," *World J. Urol.* **38**, 1895–1904 (2020).
2. M. Mossanen and J. Gore, "The burden of bladder cancer care," *Curr. Opin. Urol.* **24**, 487–491 (2014).
3. J. Leal et al., "Economic burden of bladder cancer across the European Union," *Eur. Urol.* **69**, 438–447 (2016).
4. R. Svatek et al., "The economics of bladder cancer: costs and considerations of caring for this disease," *Eur. Urol.* **66**, 253–262 (2014).
5. K. Chamie et al., "Recurrence of high-risk bladder cancer: a population-based analysis," *Cancer* **119**, 3219–3227 (2013).
6. H. Kobayashi et al., "Long term follow-up in patients with initially diagnosed low grade ta non-muscle invasive bladder tumors: tumor recurrence and worsening progression," *BMC Urol.* **14**, 5 (2014).

7. F. Placzek et al., "Morpho-molecular ex vivo detection and grading of non-muscle-invasive bladder cancer using forward imaging probe based multimodal optical coherence tomography and Raman spectroscopy," *Analyst* **145**, 1445–1456 (2020).
8. D. Bovenkamp et al., "Combination of high-resolution optical coherence tomography and Raman spectroscopy for improved staging and grading in bladder cancer," *Appl. Sci.* **8**(12), 2371 (2018).
9. K. Liang et al., "Endoscopic forward-viewing optical coherence tomography and angiography with MHz swept source," *Opt. Lett.* **42**, 3193–3196 (2017).
10. L. Wurster et al., "Endoscopic optical coherence tomography angiography using a forward imaging piezo scanner probe," *J. Biophotonics* **12**, e201800382 (2019).
11. S. Kretschmer, Ç. Ataman, and H. Zappe, "Glass 3D printing for ultra-miniaturized endoscopic optical systems," in *24th Microopt. Conf. (MOC)*, pp. 76–77 (2019).
12. Y. Taeye et al., "Manufacturing and assembly of an all-glass OCT microendoscope," *J. Micromech. Microeng.* **31**, 125005 (2021).
13. E. J. Seibel and Q. Y. J. Smithwick, "Unique features of optical scanning, single fiber endoscopy," *Lasers Surg. Med.* **30**, 177–183 (2002).
14. R. Shah et al., "Compact OCT probe for flexible endoscopy enabled by piezoelectric scanning of a fiber/lens assembly," *Proc. SPIE* **10931**, 76–82, (2019).
15. S. Vilches et al., "Miniaturized Fourier-plane fiber scanner for OCT endoscopy," *J. Micromech. Microeng.* **27**, 105015 (2017).
16. D. S. Schoeb et al., "Ex-vivo evaluation of miniaturized probes for endoscopic optical coherence tomography in urothelial cancer diagnostics," *Ann. Med. Surg.* **77**, 103597 (2002).
17. M. Hermans, J. Gottmann, and F. Riedel, "Selective, laser induced etching of fused silica at high scan-speeds using KOH," *J. Laser Micro/Nanoeng.* **9**(2), 126–131 (2014).
18. G. González-Cerdas et al., "Micro-structured glass probe for endoscopic optical coherence tomography," *Proc. SPIE* **11359**, 113590I (2020).
19. S. Makita et al., "Optical coherence angiography," *Opt. Express* **14**, 7821–7840 (2006).
20. R. F. Spaide et al., "Optical coherence tomography angiography," *Prog. Retin. Eye Res.* **64**, 1–55 (2018).
21. T.-H. Tsai et al., "Endoscopic optical coherence angiography enables 3-dimensional visualization of subsurface microvasculature," *Gastroenterol. Mot.* **147**, 1219–1221 (2014).
22. A. Mariampillai et al., "Speckle variance detection of microvasculature using swept-source optical coherence tomography," *Opt. Lett.* **33**, 1530–1532 (2008).
23. M. Zhang et al., "Projection-resolved optical coherence tomographic angiography," *Biomed. Opt. Express* **7**, 816–828 (2016).
24. Y. Jia et al., "Split-spectrum amplitude-decorrelation angiography with optical coherence tomography," *Opt. Express* **20**, 4710–4725 (2012).

Biographies of the authors are not available.